

# Measurements in Film Cooling Flows With Periodic Wakes

Kristofer M. Womack

Ralph J. Volino  
e-mail: volino@usna.edu

Mechanical Engineering Department,  
United States Naval Academy,  
Annapolis, MD 21402

Michael P. Schultz  
Naval Architecture and Ocean  
Engineering Department,  
United States Naval Academy,  
Annapolis, MD 21402

*Film cooling flows subject to periodic wakes were studied experimentally. The wakes were generated with a spoked wheel upstream of a flat plate. Cases with a single row of cylindrical film cooling holes inclined at 35 deg to the surface were considered at blowing ratios of 0.25, 0.50, and 1.0 with a steady freestream and with wake Strouhal numbers of 0.15, 0.30, and 0.60. Temperature measurements were made using an infrared camera, thermocouples, and constant current (cold-wire) anemometry. Hot-wire anemometry was used for velocity measurements. The local film cooling effectiveness and heat transfer coefficient were determined from the measured temperatures. Phase locked flow temperature fields were determined from cold-wire surveys. Wakes decreased the film cooling effectiveness for blowing ratios of 0.25 and 0.50 when compared to steady freestream cases. In contrast, effectiveness increased with Strouhal number for the 1.0 blowing ratio cases, as the wakes helped mitigate the effects of jet lift-off. Heat transfer coefficients increased with wake passing frequency, with nearly the same percentage increase in cases with and without film cooling. The time resolved flow measurements show the interaction of the wakes with the film cooling jets. Near-wall flow measurements are used to infer the instantaneous film cooling effectiveness as it changes during the wake passing cycle. [DOI: 10.1115/1.2812334]*

## Introduction

Film cooling has been studied extensively for over four decades, but most investigations have focused on flows with steady inflow conditions. The flow in a gas turbine engine, however, is inherently unsteady. Some unsteadiness results from nonuniformity in the flow exiting the combustor, which has been considered in some recent studies (e.g., Varadarajan and Bogard [1]). Turbine flows also have high freestream turbulence, which increases mixing between the main and cooling flows. This tends to cause faster dispersion of the coolant away from the surface, leading to lower film cooling effectiveness  $\eta$  and higher heat transfer coefficients, both of which reduce the benefits of film cooling. High freestream turbulence can also increase  $\eta$  in some cases, however, by increasing lateral spreading of the coolant from discrete holes. If film cooling jets lift off a surface, as is possible at high blowing ratios, high freestream turbulence can also help bring coolant back toward the surface. Several studies have examined high freestream turbulence effects, including Bons et al. [2], Kohli and Bogard [3], Ekkad et al. [4], and Burd et al. [5].

Another source of unsteadiness is the interaction between vane and blade rows in the turbine. Upstream airfoils shed wakes, which periodically impinge on the airfoils downstream. The wakes include a mean velocity deficit and increased turbulence, with effects similar to those of the increased freestream turbulence noted above. Wakes can disrupt film cooling jets, reducing the film cooling effectiveness in some areas and possibly enhancing it in others. Wake induced turbulence may also increase heat transfer coefficients, thereby reducing the overall benefit of film cooling. Airfoils passing both upstream and downstream of a turbine passage also cause periodic flow blockage, inducing pressure fluctuations which may cause film cooling jets to pulsate. None of these potentially important effects are captured in steady flow experiments. The incomplete knowledge of unsteady cooling flow behavior is typically overcome by supplying enough cooling air to prevent damage to all components in the turbine. This can lead to

overcooling in some areas, reducing engine efficiency. While steady flow studies have resulted in great advances in engine cooling, unsteady flow studies, particularly those which capture transient behavior, may lead to more efficient use of cooling air and increased engine efficiency.

A few studies have investigated the effect of wakes on film cooling. Funazaki et al. [6,7] considered flow around the leading edge of a blunt body subject to wakes produced by an upstream spoked wheel. They provide time averaged film cooling effectiveness results and note that the wakes tended to reduce  $\eta$  particularly at low blowing rates. When the cooling jet momentum was high, particularly if the jets lifted off the surface, the wake effect was reduced. Ou et al. [8] and Mehendale et al. [9] used a linear cascade with a spoked wheel to generate wakes. They note that heat transfer coefficients increased and film cooling effectiveness decreased with increased wake strength. Jiang and Han [10] similarly used a linear cascade with a spoked wheel, and present time averaged effectiveness results. They studied the effect of coolant injection from multiple hole locations in the showerhead region and on both sides of their airfoil. Results varied, depending on jet location, blowing ratio, the tendency of the coolant jets to lift off at each location, and jet density. High freestream turbulence resulted in lower effectiveness in all cases. Ekkad et al. [4] conducted a similar study and present film cooling effectiveness and local time averaged Nusselt numbers. They note that in the presence of very high freestream turbulence, the additional effect of periodic wakes is relatively small. Du et al. [11,12] also utilized a cascade and spoked wheel. They used a transient liquid crystal technique to obtain detailed time averaged film cooling effectiveness and Nusselt number distributions from an airfoil surface. They note that the wake effect on Nusselt numbers is small, but that wakes have a significant effect on film cooling effectiveness. Teng et al. [13–15] used a similar facility and also documented film cooling effectiveness and Nusselt numbers. They also used a traversing cold-wire probe to measure the flow temperature in planes downstream of the film cooling holes. They present time averaged mean and fluctuating temperature results. The unsteady wakes caused a faster dilution of the coolant jet. Higher blowing rates also result in more rapid mixing. The effects of wakes and blowing ratio on boundary layer transition were also reported. Heidmann et al. [16] used a rotating facility to investigate the

Contributed by the International Gas Turbine Institute of ASME for publication in the JOURNAL OF TURBOMACHINERY. Manuscript received June 6, 2007; final manuscript received June 22, 2007; published online July 31, 2008. Review conducted by David Wisler. Paper presented at the ASME Turbo Expo 2007: Land, Sea and Air (GT2007), Montreal, Quebec, Canada, May 14–17, 2007.

effect of wakes on showerhead film cooling. They report time averaged film effectiveness. The geometry tended to prevent jet lift-off, so  $\eta$  increased with blowing ratio. Higher wake passing rates skewed the coolant distribution, producing higher effectiveness on the pressure side of the airfoil and lower effectiveness on the suction side. Wolff et al. [17] utilized a three blade linear cascade in a high speed facility with one row of cooling holes on the suction side and one row on the pressure side of their center blade. Wakes were generated with rods fastened to belts which traveled around the cascade and two pulleys. Phase averaged velocity and turbulence levels were documented in multiple planes on both sides of the airfoil. The locations of the coolant jets were surmised from the mean velocity deficit and the turbulence level in the boundary layer. The effect of the pressure side coolant jets was reinforced by the passing wakes. On the suction side, the coolant jets were disrupted and nearly disappeared when the wake passed, but then recovered between wake passings. Adami et al. [18] did numerical simulations of the flow through this cascade.

While the above studies provide valuable information concerning the time averaged effects of wakes on film cooling, and a few provide time averaged flow field documentation, there is little information about the transient flow behavior during wake passing events. Such information could be valuable. If it is learned that film cooling jets provide effective coverage of the surface during part of the wake passing cycle but are dispersed as the wake passes, a change in design might be warranted to provide better coverage over the full cycle. Alternatively, the jets might be turned off during part of the cycle to only provide coolant when it is effective. Since film cooling jets pulse naturally in response to pressure fluctuations in the engine, it might be possible through clocking to time the jet pulses favorably with respect to wake passing events.

In the present study, film cooling jets were subject to wakes generated with upstream rods. The geometry consisted of a flat plate with a single row of five streamwise oriented round holes inclined at 35 deg to the surface. The holes were spaced  $3D$  apart, center to center, with a length to diameter ratio  $L/D=4$ . The geometry has been used in many studies including Bons et al. [2], Burd and Simon [19], Schmidt et al. [20], Pedersen et al. [21], Kohli and Bogard [22], Sinha et al. [23], and Pietrzyk et al. [24]. Blowing ratios of 0.25, 0.5, and 1.0 were investigated with various wake passing frequencies. Phase averaged flow temperature distributions, and time averaged film cooling effectiveness and heat transfer results are presented below.

## Experimental Facility and Measurements

Experiments were conducted in the facility used by Coulthard et al. [25–27]. It consists of an open loop subsonic wind tunnel with a test plate at the exit of the contraction, and a plenum to supply the film cooling jets. The wind tunnel, shown in Fig. 1, was comprised of a blower, a diffuser with three screens, a heat exchanger to maintain air nominally at 20°C, a honeycomb, a settling chamber with three screens, and a nozzle with an 8.8 area reduction. The nozzle exit area was  $0.38 \times 0.10 \text{ m}^2$ . The exiting mainstream air was uniform in temperature and velocity to within 0.1°C and 1%, respectively. The freestream turbulence intensity at the nozzle exit was 1%. This value is lower than typical intensity levels in engines. Air exiting the nozzle forms a wall jet at  $U_\infty=8 \text{ m/s}$  along the flat plate test wall. The mainstream velocity remained at  $8 \text{ m/s}$   $18D$  downstream of the film cooling holes. At this downstream location, the velocity outside the boundary layer was uniform up to the edge of the free shear layer, which was located  $3D$  from the wall. The freestream unsteadiness level gradually increased in the streamwise direction to 6%. This increase is due to the growth of the shear layer at the edge of the wall jet. Spectral measurements indicate that the freestream fluctuations are nearly all at frequencies between 5 Hz and 50 Hz, with a peak at 22 Hz. These low frequencies are associated with large scale structures formed in the shear layer, which buffet the

boundary layer but do not promote significant turbulent mixing. The boundary layer is therefore expected to behave as if subject to low freestream turbulence, and the heat transfer coefficient results by Coulthard et al. [27] are typical of low freestream turbulence conditions. The wall jet configuration is based on the facility of Burd and Simon [19].

The film cooling supply plenum was a box with  $0.38 \times 0.18 \times 0.36 \text{ m}^3$  inside dimensions. It was supplied by a manifold connected to a high pressure air source. The supply pressure was adjusted to vary the blowing ratio from  $B=0.25$  to 1.0. The air passed through small diameter valves which choked the flow between the manifold and the plenum. For a given supply pressure, the film cooling mass flow remains constant, independent of downstream conditions. Nine valves operating in parallel provided the desired coolant mass flow. The plenum contained a finned tube heat exchanger, midway between the valves and the film cooling holes. Warm water at 30°C circulated through the tubes and the air from the valves passed over the tubes, maintaining the temperature of the coolant jets at approximately 27°C.

The test wall was constructed of polyurethane foam with a thermal conductivity of 0.03 W/mK. The dimensions were 0.38 m wide, 44 mm thick, and 1.17 m long, with a starting length of  $13.3D$  upstream of the row of film cooling holes. A wall opposite the starting length and sidewalls along the length of the test wall, as shown in Fig. 1(b), helped limit interaction between the wind tunnel flow and the still air in the room. Foil heating elements were placed on the foam surface to provide a uniform heat flux condition, and are described in more detail by Coulthard et al. [25,27]. Heaters were located both upstream and downstream of the film cooling holes. The heaters were covered with a 0.79 mm thick sheet of black Formica® laminate to provide a smooth test surface. The film cooling geometry consisted of a single row of five round holes inclined at 35 deg to the surface. The sharp edged holes had a diameter of  $D=19.05 \text{ mm}$ , were spaced  $3D$  apart, center to center, and had a length to diameter ratio  $L/D=4$ . A 1.6 mm thick trip was installed  $11D$  upstream of the leading edge of the film cooling holes, and a velocity profile acquired  $0.8D$  upstream of the holes confirmed that the boundary layer was fully turbulent.

A wake generator, consisting of a spoked wheel, was installed for the present study between the contraction and the test plate. The test wall was moved 6.4 cm downstream of the contraction exit, and a 30 cm diameter, 2.5 cm thick aluminum hub was installed on an electric motor, just below the gap between the contraction and test plate. The axis of the rotation was parallel to the main flow direction. The hub had 24 threaded holes around its circumference, into which 38 cm long, 1.905 cm diameter hollow aluminum rods could be installed. When the hub was rotated, the rods cut through the main flow, generating wakes. The rods were intended to simulate the effect of the wakes shed from the trailing edges of upstream airfoils. In an engine, the diameter of an airfoil trailing edge is of the same order as the diameter of typical film cooling holes. The rods in the present study, therefore, were chosen to have the same diameter as the film cooling holes in the test plate. The wake passing velocity in a turbine is of the same order as the main flow velocity, so the rotation speed of the spoked wheel was set at 200 rpm, which produced rod velocities of 8 m/s at the spanwise centerline of the test section. Combinations of 3, 6, and 12 rods were used to produce wake passing frequencies of 10 Hz, 20 Hz, and 40 Hz. When nondimensionalized using the rod diameter and main flow velocity, these frequencies correspond to Strouhal numbers,  $Sr=2\pi fD/U_\infty$ , of 0.15, 0.30, and 0.60. These  $Sr$  are typical of engine conditions and match the range considered by Heidmann et al. [16]. The direction of rotation was set so that the rods moved toward the test plate (clockwise when looking upstream in Figs. 1(b) and 1(c)), to simulate wakes impacting the suction side of an airfoil.

For safety, the wake generator was enclosed in a plywood box, as shown in Fig. 1(b), with a rectangular hole of the contraction

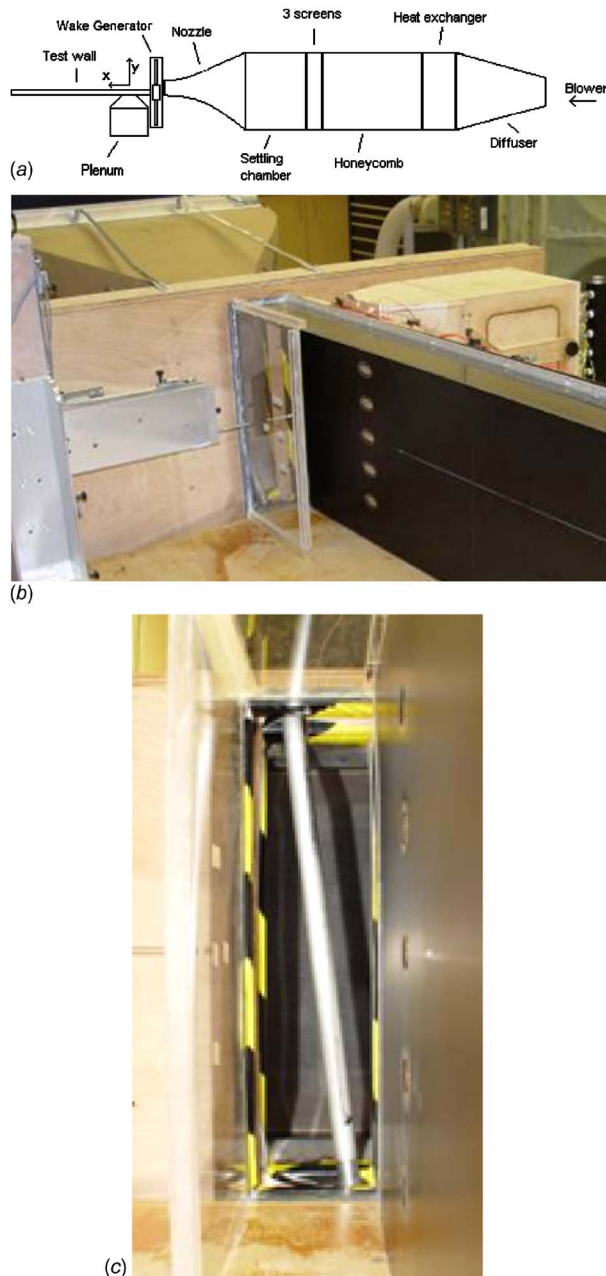


**Fig. 1 Wind tunnel configuration: (a) schematic, (b) photograph of test wall with sidewalls, and (c) photograph looking upstream at rod moving across main flow**

exit dimension to allow the main flow to pass through. The moving rods entrained air, producing a rotating flow within the box. To prevent this secondary flow from influencing the main flow, a set of rubber flaps were installed on the inside of the box, perpendicular to the direction of rod rotation and covering the plane where the rods entered the main flow. The rods pushed through the flaps, but between rods, the flaps closed, blocking the secondary flow.

**Measurements.** Thermocouples were placed in the film cooling plenum, at the plenum-side end of the outermost film cooling hole, at the wind tunnel exit, on the back of the test plate, in the ambient air, on the wall of the room to measure the surrounding temperature for radiation corrections, and in ice water as a reference. Constant current (cold-wire) and constant temperature (hot-wire) anemometry were used to measure flow temperature and velocity, respectively. Boundary layer probes with  $1.27 \mu\text{m}$  diam-

eter platinum sensors (TSI model 1261A-P.5) were used for temperature measurements, and boundary layer probes with  $3.81 \mu\text{m}$  diameter tungsten sensors (TSI model 1218-T1.5) were used for the velocity. An infrared (IR) camera (FLIR Systems Merlin model) with a Stirling cooled detector was used to measure the surface temperature field of the test wall. The temperature resolution of the camera was  $0.05^\circ\text{C}$ . The camera had a  $255 \times 318$  pixel detector and was positioned such that each pixel corresponded to a  $1 \times 1 \text{ mm}^2$  area on the test wall. The field of view on the test wall corresponded to  $13.4D \times 16.7D$ . The emissivity of the test wall was measured to be 0.95 and used in radiation corrections.

The film cooling effectiveness and Stanton number were defined, respectively, as follows.

$$\eta = \frac{T_{\text{aw}} - T_\infty}{T_{\text{jet}} - T_\infty} \quad (1)$$

$$\text{St} = \frac{q''_{\text{conv}}}{\rho C_p U_\infty (T_w - T_{\text{aw}})} \quad (2)$$

The jet, freestream, and wall ( $T_w$ ) temperatures were measured. The convective heat flux,  $q''_{\text{conv}}$ , was determined based on the power input to the heaters, with corrections for conduction and radiation losses. Measurements were made for each flow condition with the wall heaters on and off, to determine local  $T_{\text{aw}}$ ,  $\eta$ , and  $\text{St}$ . The procedure is described in more detail by Coulthard et al. [27]. Stanton numbers were determined for cases with film cooling ( $\text{St}_f$ ), and in cases without film cooling ( $\text{St}_o$ ) but otherwise similar main flow, wake, and surface heating conditions. Stanton number ratios ( $\text{St}_f/\text{St}_o$ ) were then computed to determine the effect of film cooling on heat transfer coefficients.

The thermocouples and IR camera were calibrated against a precision blackbody source, and the cold-wire probe was calibrated against the thermocouples. The uncertainty in the measured temperature was  $0.2^\circ\text{C}$ , and the uncertainty in the measured velocity was 3%. The uncertainty in the film cooling effectiveness was determined to be 6% and the uncertainty in the Stanton number is 8%. The uncertainty in the ratio of two Stanton numbers is 11%, based on a standard propagation of error with a 95% confidence interval.

Velocity profiles were measured along the centerline of the test wall at three streamwise locations,  $x=0D$ ,  $7D$ , and  $14D$ , where the origin for the coordinate system is the wall surface at the downstream edge of the center film cooling hole. The film cooling jets were off and the holes covered with thin tape during these measurements. Profiles were acquired for all three wake passing frequencies. Three-dimensional surveys of the flow temperature were measured using the cold-wire probe. Each survey consisted of a  $29 \times 11 \times 5$  grid with 1595 measurement locations. In the streamwise direction, 29 evenly spaced locations extended from  $x = -1.74D$  (the leading edge of the film cooling holes) to  $12.2D$ . In the wall normal direction, there were 11 evenly spaced locations extending from  $y=0D$  to  $2.55D$ . Coulthard et al. [26] confirmed that the flow was symmetric about the spanwise centerline in this facility, so spanwise locations were all on one side of the centerline, with five evenly spaced points extending from  $z=0$  to the midpoint between adjacent holes at  $z=1.5D$ . An infrared sensor was located in the wake generator box to detect the passing of the wake generator rods. The pulse train from this sensor was digitized along with the instantaneous anemometer voltages (13 s long traces at 10 kHz sampling rate) to allow phase averaging of the flow velocities and temperatures relative to the wake passing events. Phase averaged results were computed at 24 increments during the wake passing cycle.

**Flow Conditions.** As documented by Coulthard et al. [27] before installation of the wake generator, the boundary layer  $0.8D$  upstream of the film cooling hole leading edge had a momentum

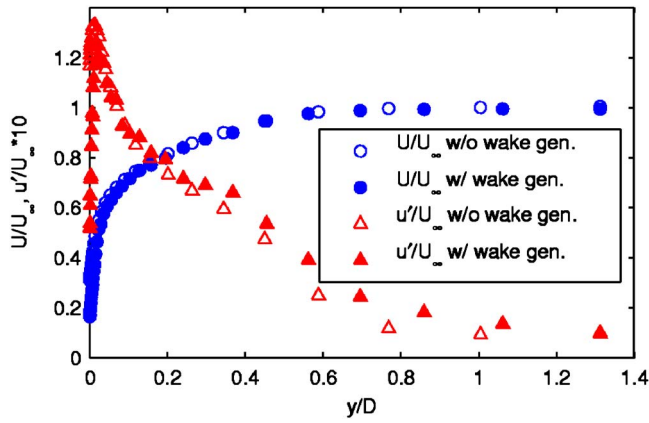


Fig. 2 Mean and fluctuating streamwise velocity upstream of film cooling holes, before installation of wake generator and during undisturbed phase of cycle with  $Sr=0.15$

thickness Reynolds number of 550 and a shape factor of 1.48. The local skin friction coefficient at this location was  $5.4 \times 10^{-3}$  and the enthalpy thickness Reynolds number was 470. The Reynolds number based on hole diameter and mainstream velocity was 10,000. Data for cases without wakes shown below were acquired without the wake generator present. With the wake generator added, the gap between the contraction exit and the leading edge of the test plate created a disturbance, which increased the thickness of the boundary layer on the test wall in cases without wakes. With the wake generator spinning, however, the rods entrained a flow into the gap, sucking off the boundary layer upstream of the test plate. The result, as shown in Fig. 2, was a boundary layer, which at the phases between wake disturbances matched the boundary layer measured by Coulthard et al. [26]. To separate the turbulence from the wake passing unsteadiness, the turbulence values shown in Fig. 2 and in the figures below are based on fluctuations from the phase averaged mean as opposed to the time averaged mean of the full data trace.

Figure 3 shows the phase averaged mean velocity at  $x=0$  for the lowest Strouhal number,  $Sr=0.15$ , case. The horizontal axis indicates the phase,  $t/T$ , where  $T$  is the wake passing period. The time  $t/T=0$  in this figure is set by the rod passing the infrared sensor in the wake generator box. The vertical axis indicates distance from the wall. The freestream velocity is set to  $U_\infty=8$  m/s, and this value is used to normalize all mean and fluctuating velocities. Far from the wall, there is a velocity deficit associated with the wake. Close to the wall, the wake causes a rise in velocity to about  $1.2U_\infty$ . The effect of the wake on the phase averaged turbulence level for this case is shown in Fig. 4. Very near the wall, for most of the cycle, the turbulence level is low due to damping in the viscous sublayer. Just above the sublayer, the fluctuation level is higher across the full cycle in the turbulent bound-

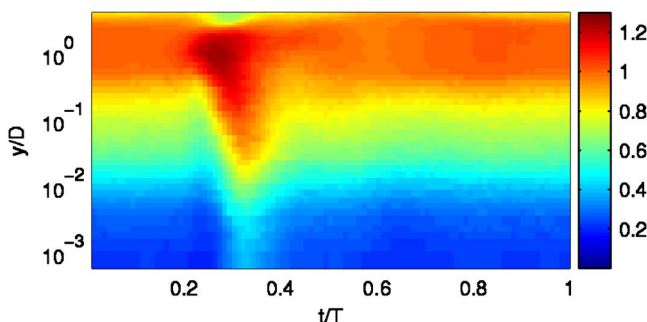


Fig. 3 Phase averaged  $U/U_\infty$  at  $x/D=0$ ,  $Sr=0.15$

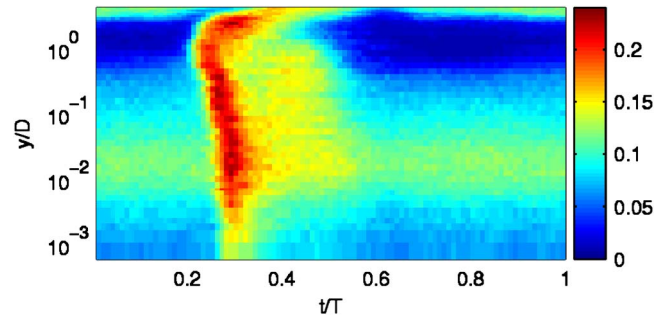


Fig. 4 Phase averaged  $u'/U_\infty$  at  $x/D=0$ ,  $Sr=0.15$

ary layer. Still farther from the wall, the freestream flow is calm for most of the cycle with 1% turbulence intensity. At the farthest locations from the wall, there are high fluctuation levels in the shear layer between the wall jet and the still air in the room. The location of the wake between  $t/T=0.2$  and  $0.6$  is clear. The effect of the wake extends all the way to the wall, indicating that it may have an important effect on film cooling. A wavelet spectral analysis indicated that the frequency of peak fluctuation energy within the wake was 125 Hz in the freestream and was 63 Hz in the sublayer. The corresponding integral length scales at these two locations were 9 mm and 5 mm, respectively.

Slices through the contour plot of Fig. 4 at  $y/D=0.01$  and  $y/D=1.5$  are shown in Fig. 5 along with corresponding data from the higher  $Sr$  cases. For the  $Sr=0.15$  case, the arrival of the wake induces a sudden rise in turbulence level both in the freestream and near the wall. This is followed by a more gradual decline to the undisturbed level between wakes. The peak freestream turbulence intensity within the wake is about 19%. Between wakes, the value drops to the 1% background level of the wind tunnel. The wake appears to occupy about 40% of the cycle, extending from about  $t/T=0.2$  to  $0.6$ . The arrival of the wake near the wall is somewhat delayed relative to the freestream, as might be expected given the lower convective velocity near the surface. The region of strong wake influence near the wall extends from about  $t/T=0.25$  to  $0.40$ . At the higher Strouhal numbers, the wake still occupies about the same amount of time in seconds, since the wake generator turns at the same speed in all cases, but it occupies a larger fraction of the wake passing period. For the  $Sr=0.3$  case, there is still a sudden rise in turbulence when the wake arrives and a short period of calm flow between wakes. For the  $Sr=0.6$  case, the wakes occupy the full cycle, so there is no clear calm period

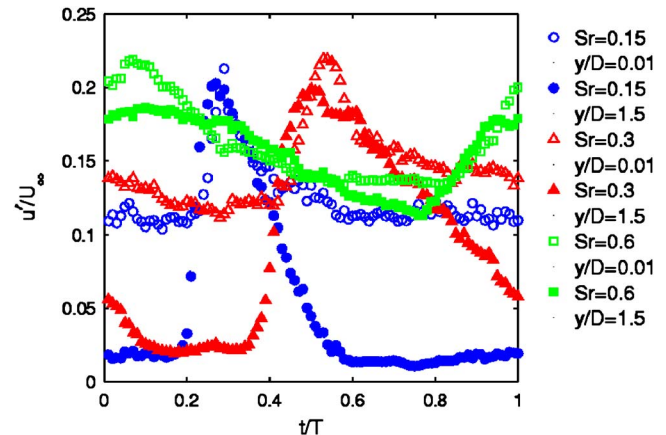
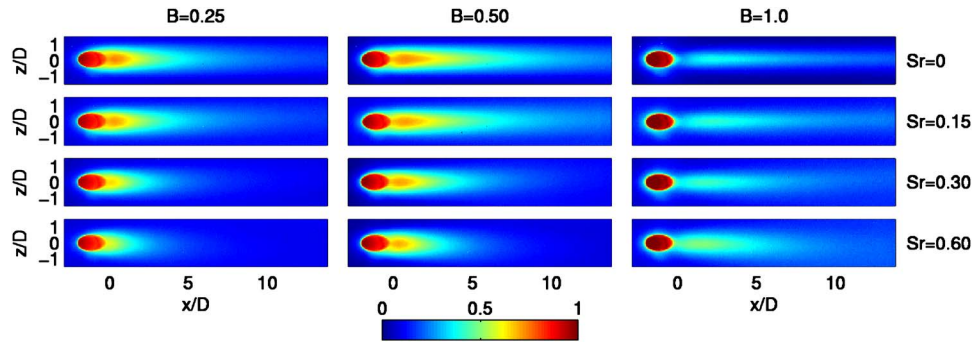


Fig. 5 Phase averaged  $u'/U_\infty$  at  $x/D=0$ ,  $y/D=0.01$  and  $1.5$  for  $Sr=0.15$ ,  $0.30$ , and  $0.60$



**Fig. 6** Film cooling effectiveness contours around center hole at various  $B$  (columns) and  $Sr$  (rows)

and the freestream turbulence level is always above 10%.

Data similar to that in Figs. 3 and 4 were acquired at  $x=7D$  and  $14D$ , and from these data, the propagation speed of the wake along the test wall was estimated. The leading edge of the wake moves at about the undisturbed freestream velocity,  $U_\infty=8$  m/s. The trailing edge of the wake is somewhat slower, at about  $0.8U_\infty$ . Near the wall, the leading and trailing edges of the disturbed flow travel at about  $0.9U_\infty$ . Using the arrival time of the wake in Fig. 5 and the propagation speed of the wake, the data in all figures shown below are shifted along the time axis so that  $t/T=0$  corresponds to the arrival of the wake at the trailing edge of the film cooling hole.

The film cooling jet velocity and temperature were documented by Coulthard et al. [26] by traversing the constant current and hot-wire probes over the hole exit plane with the main flow in the wind tunnel off. The jet temperature was very uniform and matched the plenum temperature to within  $0.2^\circ\text{C}$ . The velocity was highest in the upstream section of the hole, and agreed with the results of Burd and Simon [19], who considered the same geometry. Since the jets were only heated to approximately  $7^\circ\text{C}$  above the mainstream temperature, the density ratio of jets to mainstream was 0.98. Hence, the blowing and velocity ratios were essentially equal. Temperature and velocity measurements were compared between the five film cooling holes. The hole to hole variation in temperature was 2% of the jet to mainstream temperature difference, and velocity variation was 8% of the mainstream velocity.

For the  $Sr=0$  (no-wake) cases, the main flow and coolant flow resulted in good periodicity downstream of all five coolant holes, as shown by Coulthard et al. [26]. Similar uniformity was observed for the  $Sr=0.15$  cases. At the higher  $Sr$ , however, vortices generated at the hub and tip ends of the wake generator rods disturbed the flow around the outermost holes. To avoid these disturbances, spanwise averages were taken only about the center hole, between  $z = \pm 1.5D$ .

## Results and Discussion

**Time Averaged Film Cooling and Heat Transfer.** The effects of the wakes on film cooling effectiveness are shown in Figs. 6–9. Coulthard et al. [26] showed that the  $Sr=0$  (no-wake) cases agreed well with data from the literature. Effectiveness contours downstream of the center hole are shown for all cases in Fig. 6. Centerline and spanwise average effectiveness are shown in Figs. 7–9 for the  $B=0.25$ , 0.50, and 1.0 cases, respectively. Without wakes, the  $B=0.50$  case has the highest effectiveness. The  $B=0.25$  case has lower effectiveness because there is less coolant available to protect the surface. The effectiveness is low in the  $B=1.0$  case due to jet lift-off, as shown by Coulthard et al. [26]. The effect of the wakes is similar for the  $B=0.25$  and 0.50 cases. The wakes have little effect at  $Sr=0.15$ , but the streamwise extent of the region of effective cooling is noticeably reduced at the

higher Strouhal numbers. The wakes reduce the effectiveness by as much as 60%, with the strongest effect along the centerline. In contrast to the lower blowing ratio results, the results with  $B=1.0$  show higher effectiveness with better lateral spreading at the higher Strouhal numbers. As will be shown below, the jets exhibit considerable lift-off at this blowing ratio, and the wakes help to force the coolant back toward the wall. At the centerline, the wakes raise the effectiveness immediately downstream of the holes in the  $B=1.0$  cases by as much as 30%. There is little effect downstream of  $x/D=4$ . The spanwise average results show about a doubling of the effectiveness between the  $Sr=0$  and  $Sr=0.6$  cases at all streamwise locations. Comparing the results at the three blowing ratios, when  $Sr=0$  or 0.15, the  $B=0.5$  cases have the highest effectiveness. When  $Sr=0.6$ , the  $B=1.0$  case has the best results downstream of  $x=2D$ . For  $x>9D$ , the effectiveness in the  $B=1.0$  case is about double that in the  $B=0.5$  case. The wakes mitigate the effects of jet lift-off, and the higher total coolant volume with  $B=1.0$  produces higher effectiveness. It is noteworthy that a blowing ratio chosen based on the  $Sr=0$  results will not necessarily be most effective when wakes are present.

The effects of wakes on Stanton number are shown in Figs. 10–12. Figure 10 shows Stanton numbers for cases without film cooling. Increasing Strouhal number raises the Stanton numbers above the no-wake case by about 7%, 18%, and 36% for the  $Sr$

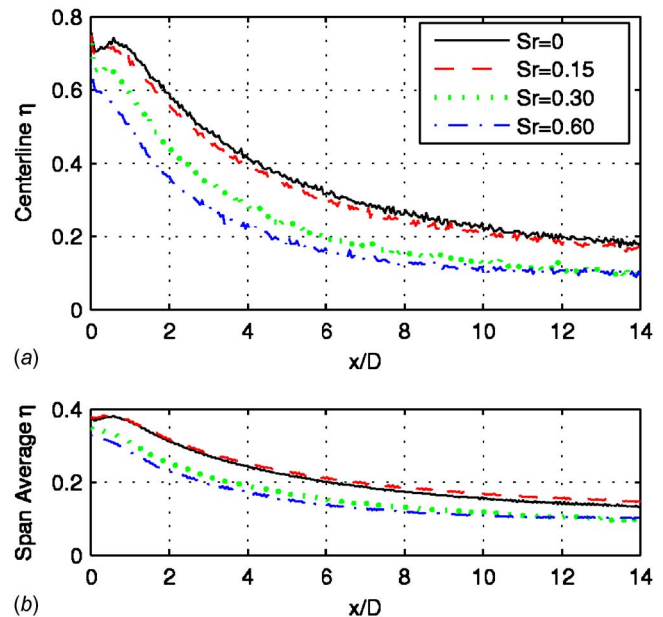


**Fig. 7** Film cooling effectiveness for  $B=0.25$  cases at various  $Sr$ ; (a) centerline and (b) spanwise averaged

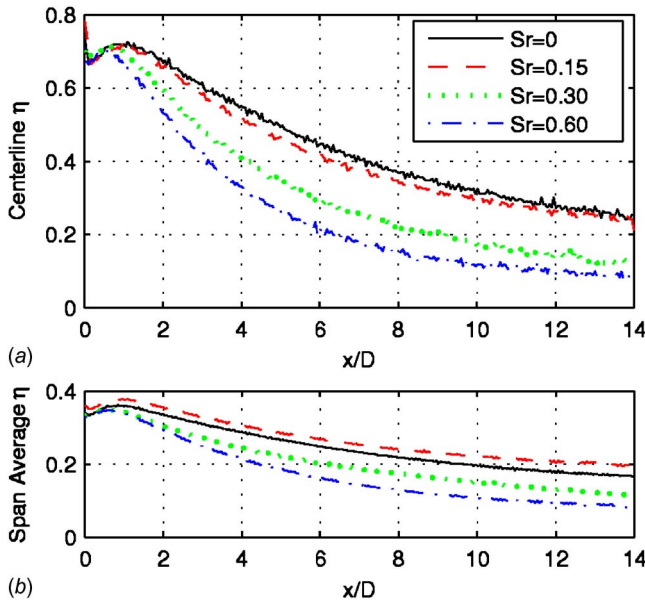


Fig. 8 Film cooling effectiveness for  $B=0.5$  cases at various  $Sr$ ; (a) centerline and (b) spanwise averaged

$=0.15, 0.30,$  and  $0.60$  cases, respectively. The increases are consistent with the effective rise in the near-wall velocity and turbulence level caused by the wakes and shown in Figs. 3–5. Stanton number ratio contours are shown in Fig. 11. Two lines of high  $St_f/St_o$ , symmetric about the spanwise centerline and extending downstream of the hole, are visible in all cases. These are believed to result from the kidney shaped vortices which form in the film cooling jets, and are discussed in more detail by Coulthard et al. [25]. Also visible are regions of high  $St_f/St_o$  extending a short distance downstream from the lateral edges of the hole. These are believed to result from the horseshoe vortex which forms when the main flow boundary layer wraps around the film cooling jet. The centerline and spanwise average  $St_f/St_o$  are shown in Figs. 12–14 for the  $B=0.25, 0.5,$  and  $1.0$  cases, respectively. In all cases, the ratio is high near the hole, but drops to near 1 by  $x$

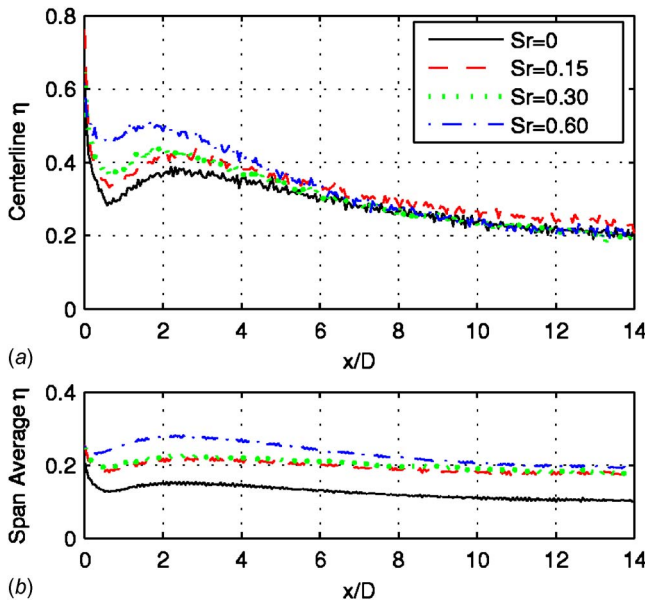


Fig. 9 Film cooling effectiveness for  $B=1.0$  cases at various  $Sr$ ; (a) centerline and (b) spanwise averaged

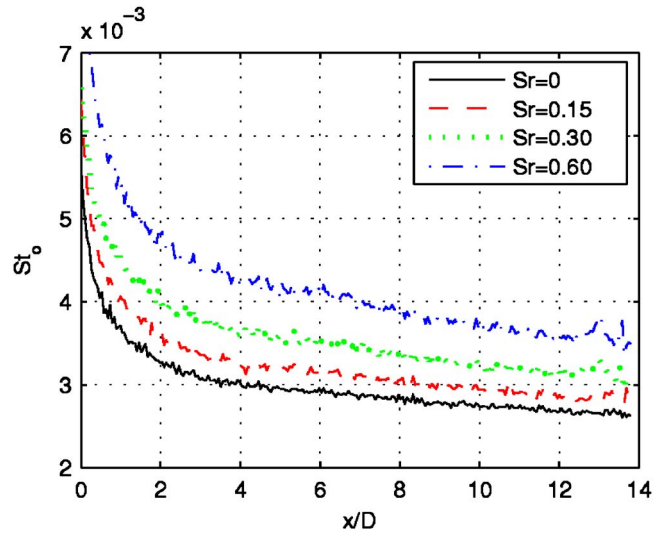


Fig. 10 Stanton numbers for cases without film cooling at various  $Sr$

$=6D$ . There appears to be a weak trend of the ratio decreasing with increasing Strouhal number, but the differences are small and within the uncertainty. The  $St_o$  values increase significantly with increasing wake frequency as shown in Fig. 10, and the wakes cause about the same percentage increase in Stanton numbers for the cases with film cooling. Hence, the Stanton number ratios do not depend strongly on Strouhal number.

The heat transfer to a surface depends on both the film cooling effectiveness and the heat transfer coefficient. The combined effect can be expressed as a heat flux ratio,

$$\frac{q''_f}{q''_o} = \frac{St_f}{St_o} \left( 1 - \frac{\eta}{\psi} \right) \quad \psi = \frac{T_w - T_\infty}{T_{jet} - T_\infty} = 0.6 \quad (3)$$

The numerical value of  $\psi=0.6$  is taken from Sen et al. [28] and others, and is a typical value for this temperature ratio under engine conditions. More discussion of the heat flux ratio for the  $Sr=0$  cases is available in Ref. [27]. Contours of  $q''_f/q''_o$  for all cases are shown in Fig. 15. Because the Stanton number ratio is near unity at most locations, the heat flux ratios of Fig. 15 reflect the effectiveness values of Fig. 6. At low Strouhal numbers,  $q''_f/q''_o$  is lowest for the  $B=0.5$  case. For the higher Strouhal numbers,  $q''_f/q''_o$  is lower for the  $B=1.0$  cases, particularly at downstream locations.

**Phase Averaged Flow Temperature.** The time averaged surface results presented above can be better explained using flow temperature data. Figure 16 shows the time averaged temperature field for the  $B=0.25, 0.5,$  and  $1.0, Sr=0$  cases. The top image in each figure shows dimensionless temperature contours,  $\phi=(T - T_\infty)/(T_{jet} - T_\infty)$ , in multiple planes arranged to provide a three-dimensional image of the temperature field. The lower image in each figure shows an isothermal surface with  $\phi=0.3$ . This value of  $\phi$  was found to give a good visual representation of the jet position. The jet clearly remains near the surface at the lower blowing ratios, and extends further downstream in the  $B=0.5$  case before being dissipated. In the  $B=1.0$  case, the jet clearly has lifted away from the surface, and although it extends farther downstream than in the other cases, it does not provide effective cooling. These results agree with the effectiveness results of Figs. 6–9.

Phase averaged flow temperature results for the  $B=0.5, Sr=0.15$  case are shown in Fig. 17. Six phases from the cycle are shown. The format and color range of the plots are the same as in Fig. 16, so some of the axis labels have been removed for clarity.

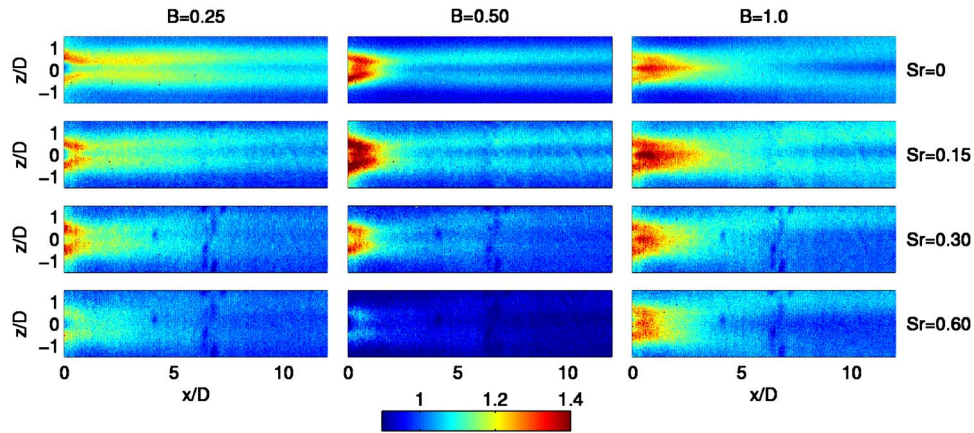


Fig. 11 Stanton number ratio,  $St_f/St_o$ , contours around center hole at various  $B$  (columns) and  $Sr$  (rows)

The start of the cycle,  $t/T=0$ , in Fig. 17(a), is set to correspond to the arrival of the leading edge of the wake at the hole location. The temperature field appears very similar to the  $Sr=0$  case of Fig. 16(b). By  $t/T=0.17$ , there appears to be a slight reduction in the effective jet diameter at about  $x=2D$ , and a slight bulge at  $x=4D$ . These locations correspond to the location of strongest near-wall wake turbulence, as indicated by the timing shown in Fig. 5. By  $t/T=0.33$ , the strong wake turbulence is located between about  $x=5$  and  $10D$ , and the jet has clearly been dispersed in this region. At  $t/T=0.5$ , the wake is beginning to move out of the field of view, and the jet has been dispersed in the downstream part of the measurement region. Also, new undisturbed jet fluid is following behind the wake. The undisturbed jet continues to extend farther downstream at  $t/T=0.67$ , and by  $t/T=0.83$ , the jet appears to have recovered to its steady state, between-wake, condition. It is

interesting that the wake is not able to disperse the jet when it first emerges from the hole, and the jet appears to remain intact between  $x=0$  and  $4D$  at all phases. It must take some small but finite time for the wake turbulence to mix the jet fluid with the main flow and begin to disperse it, and during this time, the fluid moves about  $4D$  downstream.

The behavior in the  $B=0.25$ ,  $Sr=0.15$  case is very similar to that of the  $B=0.5$  case of Fig. 17. With half the coolant volume, the lower momentum jet at  $B=0.25$  does not extend as far from the wall as in the  $B=0.5$  case, and the jet does not extend as far downstream before it is diluted by the main flow. The effect of the wake, however, appears to be the same for the two cases.

The temperature fields for the  $B=1.0$ ,  $Sr=0.15$  case are shown in Fig. 18. At  $t/T=0$ , the jet is clearly lifted off the wall, and

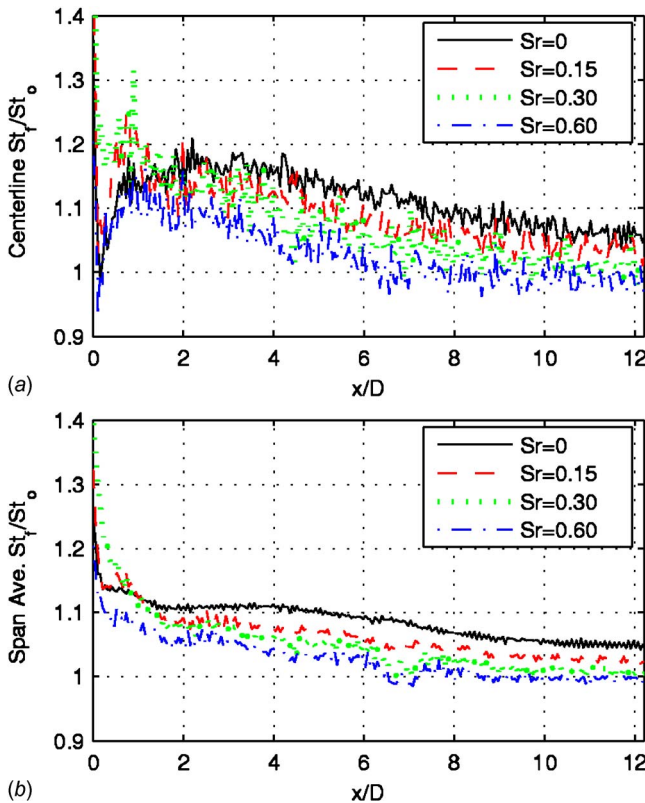


Fig. 12 Stanton number ratio,  $St_f/St_o$ , for  $B=0.25$  cases at various  $Sr$ ; (a) centerline and (b) spanwise averaged

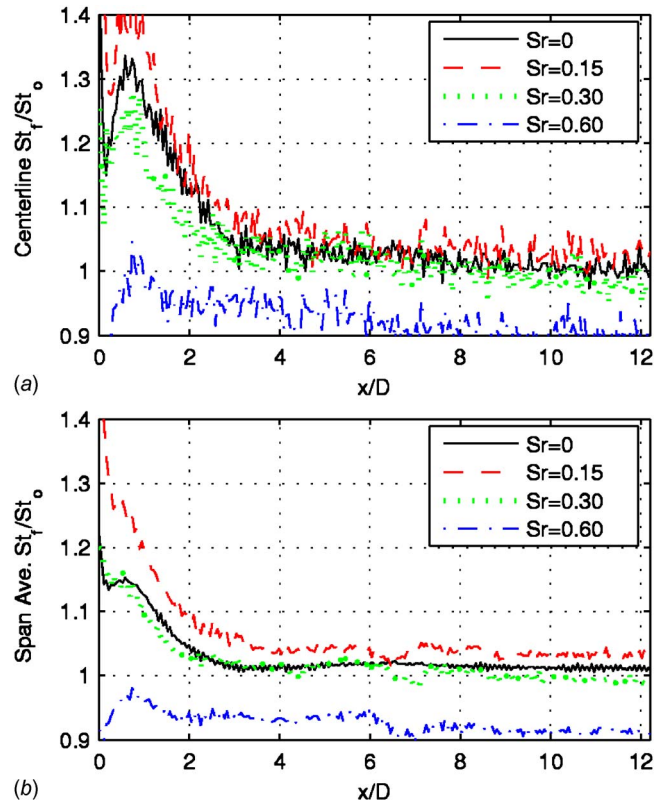


Fig. 13 Stanton number ratio,  $St_f/St_o$ , for  $B=0.5$  cases at various  $Sr$ ; (a) centerline and (b) spanwise averaged

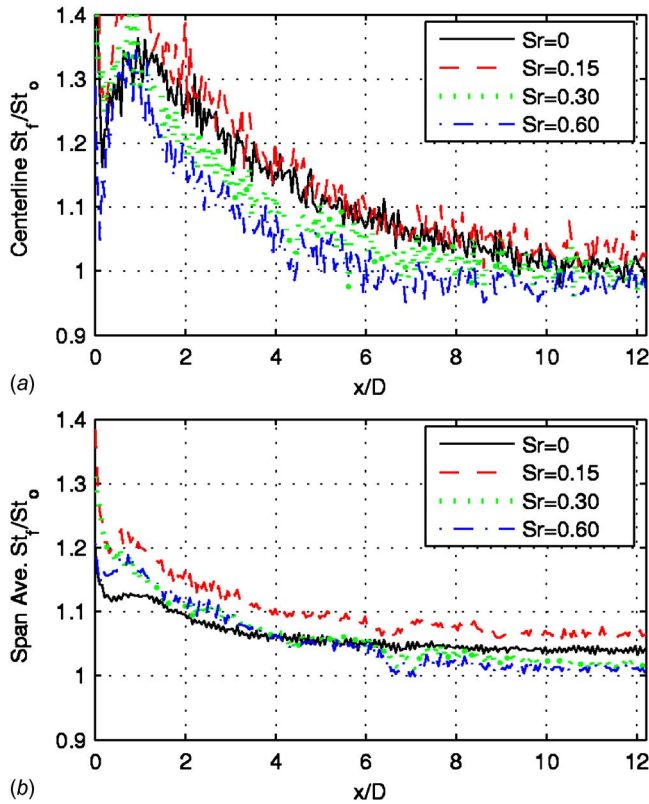


Fig. 14 Stanton number ratio,  $St_f/St_o$ , for  $B=1.0$  cases at various  $Sr$ ; (a) centerline and (b) spanwise averaged

appears essentially the same as in the  $Sr=0$  case of Fig. 16(c). At  $t/T=0.17$ , there is a bulge in the jet at  $x=4D$  as the wake passes, similar to the  $B=0.5$  case of Fig. 17(b). The upstream part of the jet also appears to be pushed closer to the wall by the wake at this phase, which would tend to momentarily increase the film cooling effectiveness. This agrees with the rise in effectiveness shown in Fig. 9, particularly for the spanwise average. At  $t/T=0.33$ , the wake has dispersed the jet between  $x=5$  and  $10D$ , as in the  $B=0.5$  case at this phase. For the remainder of the cycle, the jet recovers, as in the lower  $B$  cases, and the lift-off from the wall remains clear.

The  $B=0.5$ ,  $Sr=0.3$  case is shown in Fig. 19. The flow is moving at the same velocity as in the  $Sr=0.15$  case, but the wakes are arriving twice as frequently, so there is less time for the jet to

recover between wakes. At  $t/T=0$ , the jet is against the surface, as in Fig. 17, but does not extend as far downstream before being dispersed. It has not, at this phase, fully recovered from the previous wake. The recovery continues to  $t/T=0.17$ , even as the next wake arrives. By  $t/T=0.33$ , the jet extends even farther downstream, but it is beginning to be disturbed between  $x=2$  and  $4D$ , corresponding to the same behavior observed in Fig. 17(b) (Figs. 17(b) and 19(c) correspond to the same dimensional time after the arrival of the wake). The wake disperses the jet downstream of  $x=2D$  over the next two phases shown, and is nearly out of the measurement region by  $t/T=0.83$ , as the jet begins to recover. The jet never fully recovers, however, to the steady flow condition of Figs. 16(b), 17(a), and 17(f). In agreement with the  $Sr=0.15$  case, the jet appears to remain intact in the region immediately downstream of the hole. The film cooling effectiveness in Fig. 8 reflects this, with the effectiveness dropping only slightly between the  $Sr=0$  and 0.30 cases upstream of  $x=2D$ , but more significantly farther downstream.

Figure 20 shows the  $B=1.0$ ,  $Sr=0.30$  case. As in the  $B=0.50$  case at this Strouhal number, the jet is still recovering from the previous wake at  $t/T=0$ , the jet continues to extend farther downstream until  $t/T=0.50$ , and the disturbance of the next wake is visible between  $x=2$  and  $4D$  at  $t/T=0.33$ . The dispersal of the jet by the wake is clear between  $x=4$  and  $7D$  at  $t/T=0.5$ , and the affected region continues to move downstream at the next two phases shown, in agreement with the behavior at  $B=0.5$  in Fig. 19. Figure 20 shows that the jet has lifted off the wall, but in agreement with the observation in Fig. 18(b) for the  $B=1.0$ ,  $Sr=0.15$  case, the wake appears to push the jet back closer to the wall than in the steady flow case of Fig. 16(c). This helps to explain the increase in film cooling effectiveness at higher  $Sr$  in Fig. 9.

The  $Sr=0.6$  cases with  $B=0.5$  and  $1.0$  are shown in Figs. 21 and 22, respectively. As shown by the turbulence traces in Fig. 5, there is no recovery period between wakes at this Strouhal number. There are two wakes present in the measurement region at all phases. At  $t/T=0$  in both Figs. 21 and 22, the preceding wake is centered near  $x=6D$  as the next wake arrives at the hole. The preceding wake moves downstream at the subsequent phases and moves out of the measurement region at about  $t/T=0.67$ . The streamwise extent of the jet increases slightly during this time, as the jet begins to recover. At  $t/T=0.67$ , however, the center of the next wake has arrived at about  $x=2D$ , and it is clearly affecting the jet by  $t/T=0.83$ . Hence, there is essentially no time for the jet to recover, and there is much less variation during the cycle than at the lower Strouhal numbers. The streamwise extent of the jet before dispersal is reduced for both blowing ratios compared to the lower  $Sr$  cases. In the  $B=0.5$  case, this results in much lower

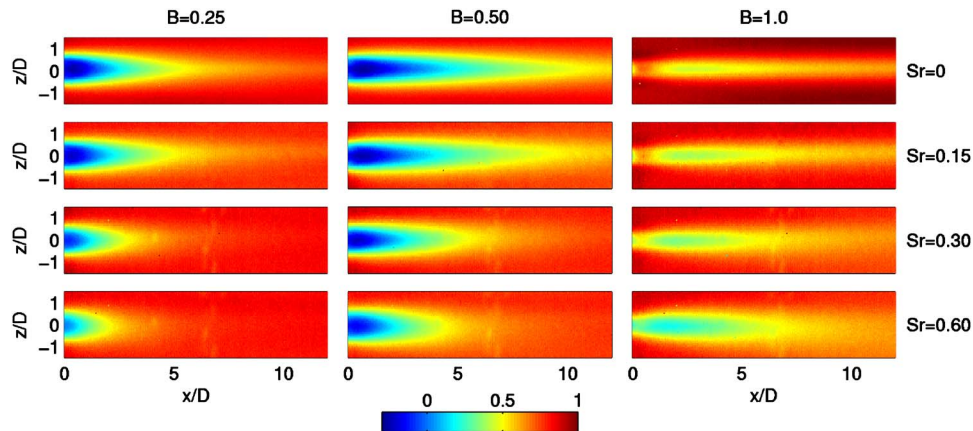


Fig. 15 Heat flux ratio,  $q''/q''_o$ , contours around center hole at various  $B$  (columns) and  $Sr$  (rows)

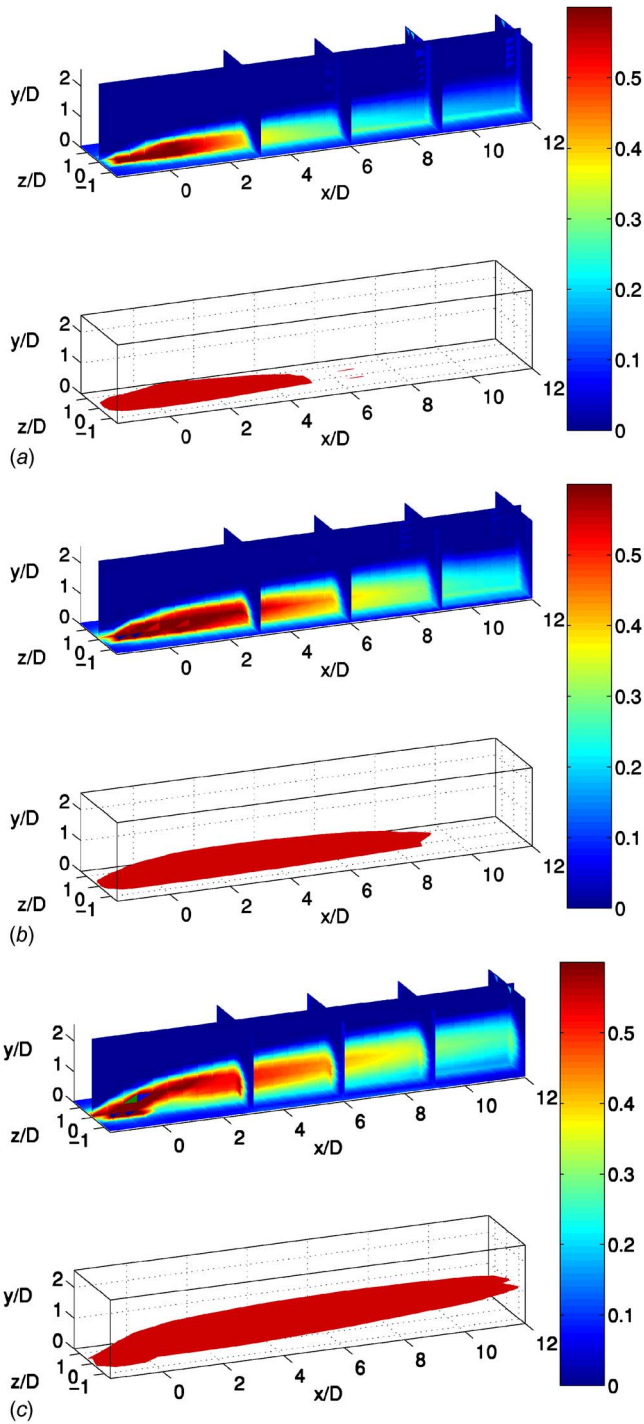


Fig. 16 Dimensionless temperature field,  $\phi$ , for steady  $Sr=0$  cases; upper image shows temperature contours in various planes, lower image shows isothermal surface with  $\phi=0.3$ ; (a)  $B=0.25$ , (b)  $B=0.5$ , and (c)  $B=1.0$

film cooling effectiveness, as shown in Fig. 8. In Fig. 22, it is clear that in addition to reducing the streamwise extent of the jet, the wake forces the jet back toward the wall during the full cycle. This raises the effectiveness, as shown in Fig. 9. The wake turbulence may cause more spreading of the jet in all directions, including laterally and toward the wall. The wake's acceleration of the near-wall flow, shown in Fig. 3, may also reduce lift-off.

**Instantaneous Film Cooling Effectiveness.** The changing flow temperature during the cycle indicates that the instantaneous film

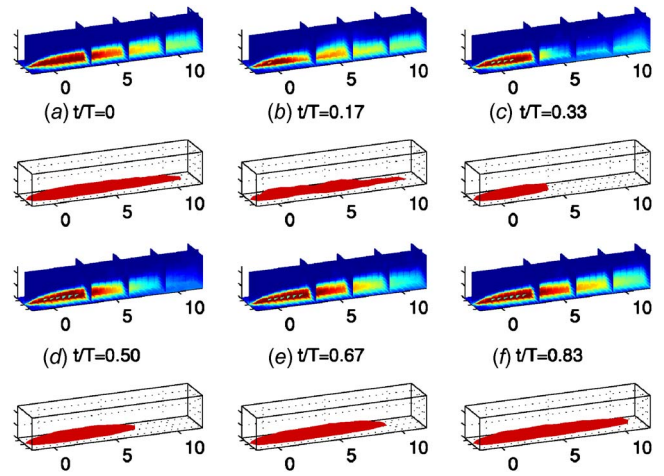


Fig. 17 Dimensionless temperature field at various phases for  $B=0.5$ ,  $Sr=0.15$  case

cooling effectiveness must also change. This cannot be measured directly with a real experimental surface, since the real surface is not perfectly adiabatic and has a nonzero heat capacity. The surface temperature cannot respond quickly enough to capture the instantaneous effects of the passing wakes. The flow temperature

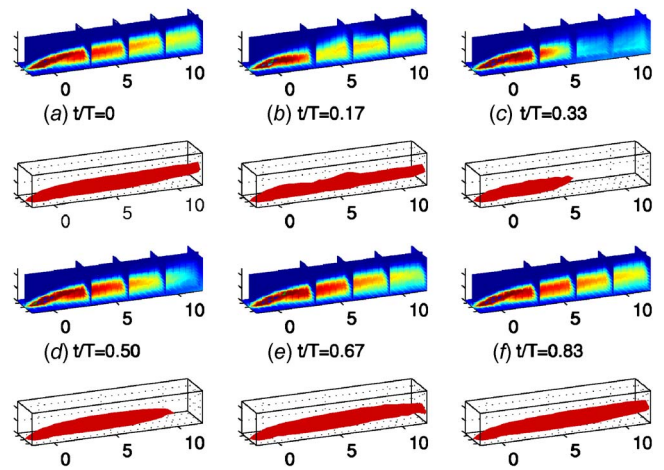


Fig. 18 Dimensionless temperature field at various phases for  $B=1.0$ ,  $Sr=0.15$  case

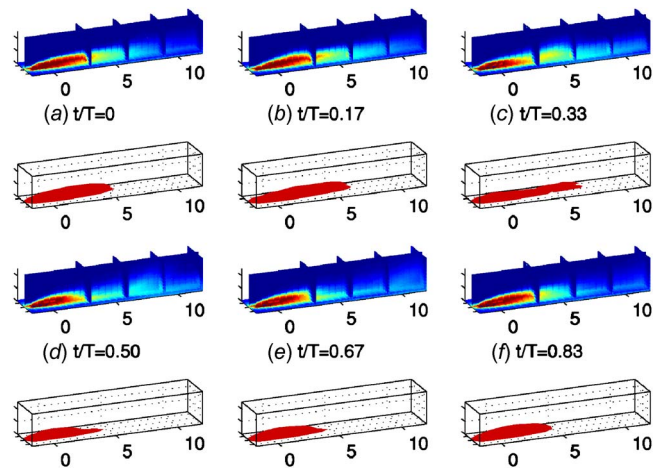


Fig. 19 Dimensionless temperature field at various phases for  $B=0.5$ ,  $Sr=0.30$  case

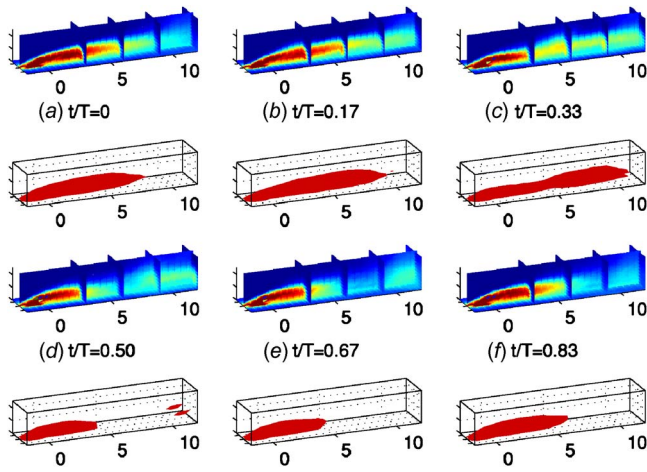


Fig. 20 Dimensionless temperature field at various phases for  $B=1.0$ ,  $Sr=0.30$  case

does respond quickly, however, as shown above, and the instantaneous flow temperature near the surface may approximate the temperature a perfectly responding surface would achieve. The approximation will not be perfect. The flow immediately adjacent to the wall will be influenced by the actual steady wall temperature. The temperature far from the wall will not be representative of the surface. Still, the instantaneous flow temperature close to the wall should give a reasonable approximation of the temperature a perfectly adiabatic wall would achieve, and it will provide insight into the unsteady film cooling effectiveness. Kohli and Bogard [22] used measured flow temperatures to extrapolate to the wall temperature and noted that the extrapolated value differed from the measured temperature at  $y/D=0.1$  by only 0.02 in  $\phi$ . In the present study, the instantaneous temperatures measured in a plane at  $y=0.08D$  are phase averaged and used to define the approximate unsteady film cooling effectiveness as

$$\eta^* = \phi(y=0.08D) = \frac{T(y=0.08D) - T_\infty}{T_{\text{jet}} - T_\infty} \quad (4)$$

Figure 23 shows contours of the effectiveness,  $\eta$  (lower half of plot), and the time average of the approximation,  $\eta^*$  (upper half of plot), for the  $B=0.5$ ,  $Sr=0.30$  case. The agreement between  $\eta$  and  $\eta^*$  is good. The same good agreement was generally observed at the other blowing ratios and Strouhal numbers. More comparisons are presented below. The good time averaged agreement provides

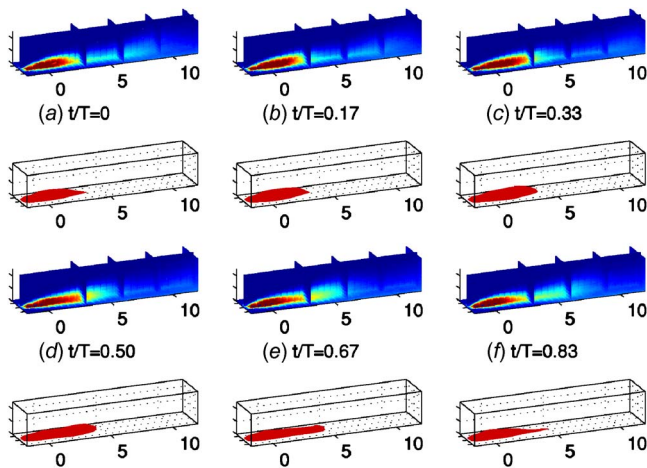


Fig. 21 Dimensionless temperature field at various phases for  $B=0.5$ ,  $Sr=0.60$  case

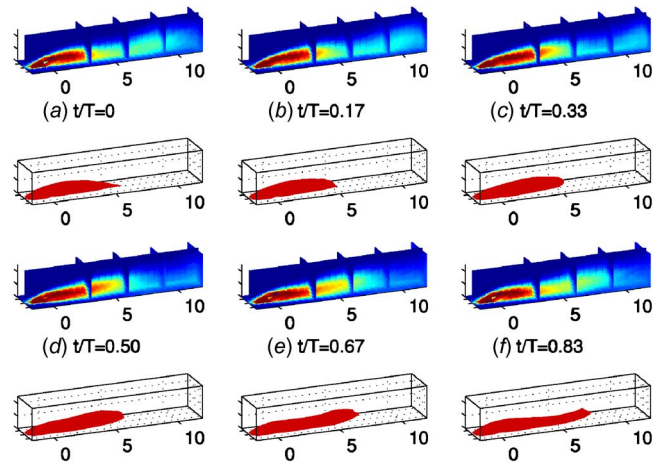


Fig. 22 Dimensionless temperature field at various phases for  $B=1.0$ ,  $Sr=0.60$  case

confidence to proceed with study of the phase averaged  $\eta^*$  results.

Figure 24 shows a time-space plot of the phase averaged  $\eta^*$  results for the  $B=0.5$ ,  $Sr=0.15$  case. The vertical axis indicates the phase, with the data repeated to show two cycles. A horizontal line in the figure shows the centerline (Fig. 24(a)) or spanwise average (Fig. 24(b)) value of  $\eta^*$  at a particular phase. The white lines show the location of the wake, as determined from the velocity data of Fig. 4. The thicker solid line corresponds to the leading edge of the wake in the freestream, and the thinner solid line indicates the trailing edge in the freestream. The dashed lines indicate the leading and trailing edges of the period of strong wake turbulence near the wall. The value of  $\eta^*$  drops quickly after the arrival of the wake near the wall, and continues to drop until the end of the strong wake turbulence near the wall. The value then rises between wakes.

Figure 25 shows  $\eta^*$  for the  $B=1.0$ ,  $Sr=0.15$  case. At the centerline (Fig. 25(a)), for  $x > 3D$ , the effect of the wake on  $\eta^*$  is similar to that in the  $B=0.5$  case of Fig. 24. In the upstream region, however, low  $\eta^*$  indicates lift-off of the jet between wakes at  $x < 2D$ . The wakes raise  $\eta^*$  in this region by reducing lift-off, as shown in Fig. 18.

Results for the  $Sr=0.6$ ,  $B=0.5$  cases are shown in Fig. 26. As above, the thick solid line indicates the arrival of the wake in the freestream, and the dashed lines indicate the period of strong wake turbulence near the wall. The trailing edge line is not shown, however, because the effects of the preceding wake are still present in the freestream when the next wake arrives. As in the  $Sr=0.15$  case,  $\eta^*$  changes during the cycle, but the variation is not as large at the higher  $Sr$ , and timing with respect to the wake is more complicated, because the recovery from the previous wake overlaps the response to the subsequent wake. The same behavior can be seen at  $x > 3D$  in Fig. 27 for the  $Sr=0.6$ ,  $B=1.0$  case. Upstream of  $x=3D$  in the  $B=1.0$  case, the wake increases  $\eta^*$ , as

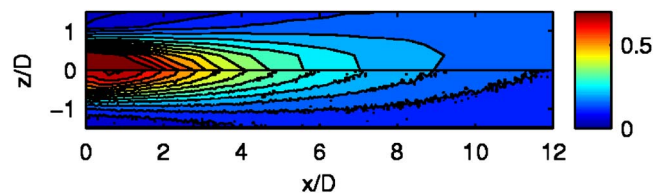


Fig. 23 Film cooling effectiveness,  $\eta$  (lower half of plot), and time averaged approximate effectiveness,  $\eta^*$  (upper half of plot), for  $B=0.5$ ,  $Sr=0.30$  case

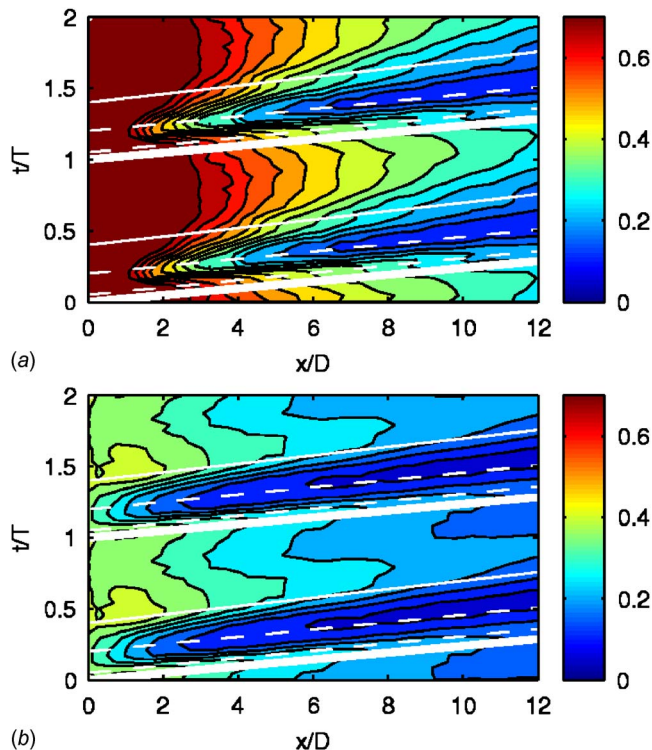


Fig. 24 Phase averaged  $\eta^*$  for  $B=0.5$ ,  $Sr=0.15$  case; (a) centerline and (b) spanwise average

in the  $Sr=0.15$  case (Fig. 25), by reducing lift-off.

The effective in-wake and between-wake values of  $\eta^*$  are extracted from the data of Figs. 24 and 26 along lines sloped according to the convection velocity and passing through the data most disturbed and least disturbed by the wakes. These results, along

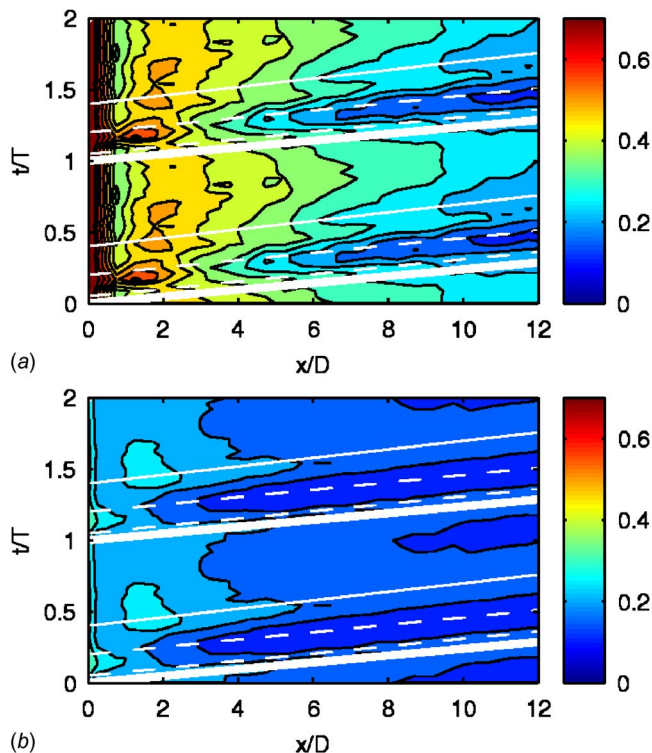


Fig. 25 Phase averaged  $\eta^*$  for  $B=1.0$ ,  $Sr=0.15$  case; (a) centerline and (b) spanwise average

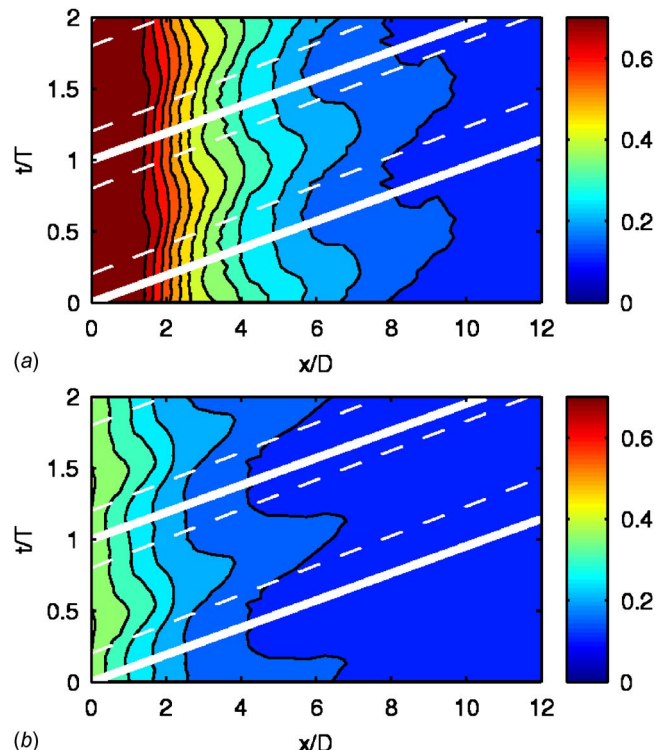


Fig. 26 Phase averaged  $\eta^*$  for  $B=0.5$ ,  $Sr=0.60$  case; (a) centerline and (b) spanwise average

with the time averaged  $\eta$  and  $\eta^*$  for all Strouhal numbers, are shown in Fig. 28 for the  $B=0.5$  cases. At the centerline (Fig. 28(a)), the agreement between the time averaged  $\eta^*$  and  $\eta$  is good at all  $Sr$ . At  $Sr=0.15$ , the in-wake  $\eta^*$  is more than 50% lower than the between-wake value. The between-wake results agree well with the  $Sr=0$  case values, indicating that the flow is able to recover to the undisturbed state between wakes. The in-wake values at  $Sr=0.15$  agree well with the  $Sr=0.30$  and  $0.60$  results, suggesting common behavior for the disturbed flow. The differences between the in-wake and between-wake  $\eta^*$  are smaller for the  $Sr=0.30$  and  $0.60$  cases because the flow does not have time to recover to an undisturbed state between wakes. The spanwise average results (Fig. 28(b)) show the same trends as the centerline results, but the differences between cases and phases are smaller. Differences for the  $B=1.0$  cases, as shown in Figs. 25 and 27, are of the order of the experimental uncertainty. The time averaged effectiveness is generally lower with  $B=1.0$  than with  $B=0.5$ , which tends to make differences smaller as well. The wakes also increase mixing while reducing lift-off at  $B=1.0$ , and these competing effects tend to reduce differences in the effectiveness.

## Conclusions

Unsteady wakes were shown to have a strong effect on the film cooling effectiveness and heat transfer for the cases considered. Stanton numbers increase significantly with wake Strouhal number. The increases were similar in cases with and without film cooling, however, so Stanton number ratios were not strongly dependent on Strouhal number. Phase averaged flow temperature measurements clearly showed how the wakes disturb the film cooling jets and the recovery between wakes. At low Strouhal numbers, the recovery was complete, and the time averaged film cooling effectiveness results differed only slightly from those in cases without wakes. At high Strouhal numbers, the time for recovery was insufficient, and the jets were disturbed throughout the cycle, resulting in 50% reductions in effectiveness with  $B=0.5$ . With  $B=1.0$ , the combined effects of reduced lift-off and in-

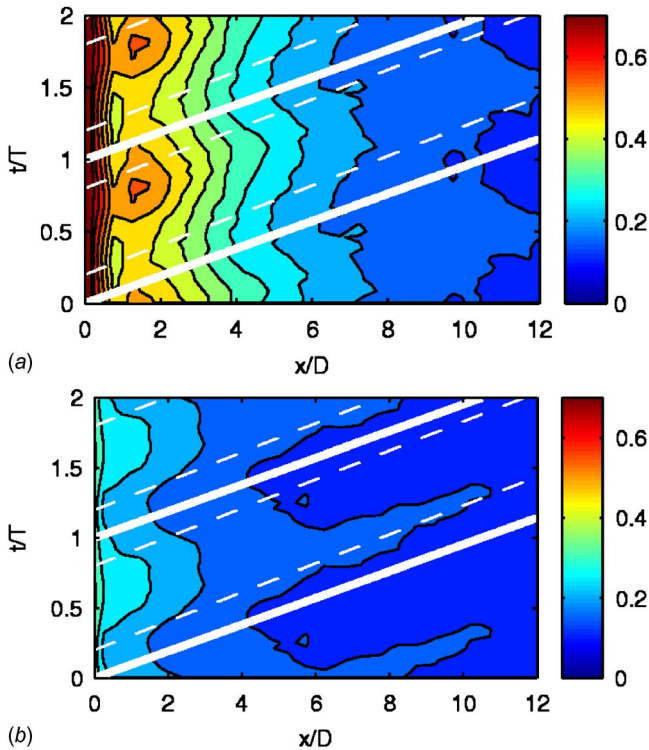


Fig. 27 Phase averaged  $\eta^*$  for  $B=1.0$ ,  $Sr=0.60$  case; (a) centerline and (b) spanwise average

creased mixing resulted in little variation of the centerline effectiveness with Strouhal number. Enhanced lateral spreading, however, resulted in noticeable increases with  $Sr$  in the spanwise average effectiveness for the  $B=1.0$  cases. Unsteady near-wall flow temperature measurements were used to approximate the unsteady film cooling effectiveness during the wake passing cycle.

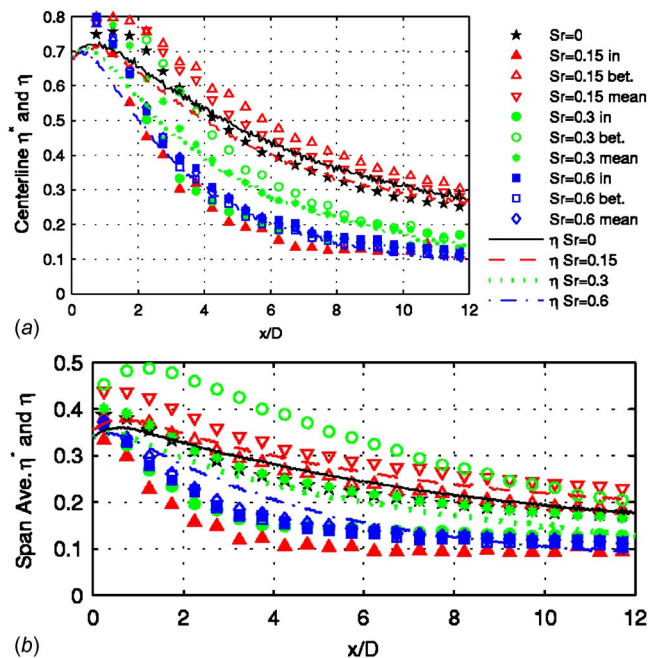


Fig. 28 Phase averaged  $\eta^*$  in wakes, between wakes, time mean of all phases, and corresponding  $\eta$  for  $B=0.5$  cases; (a) centerline and (b) spanwise average

During the wake passing, the unsteady effectiveness was low and approximately equal for cases at all Strouhal numbers. Variation during the rest of the cycle depended on the time available for recovery between wakes.

### Acknowledgment

The first author gratefully acknowledges the Office of Naval Research for partial support of this work, via the Naval Academy Trident Scholar Program, on funding Document No. N0001406WR20137. The second author gratefully acknowledges partial support by the Naval Air Systems Command.

### Nomenclature

- $B = \rho_{jet} U_{jet} / \rho_{\infty} U_{\infty}$ , blowing ratio
- $c_p$  = specific heat at constant pressure
- $D$  = film cooling hole and wake generator rod diameter
- $f$  = frequency, Hz
- $L$  = length of film cooling hole channel
- $q''$  = heat flux
- $Sr$  = Strouhal number,  $Sr = 2\pi f D / U_{\infty}$
- $St$  = Stanton number,  $q''_{conv} / [\rho c_p U_{\infty} (T_w - T_{aw})]$
- $T$  = temperature or wake passing period
- $t$  = time
- $U$  = velocity
- $u'$  = phase averaged rms streamwise velocity
- $x$  = streamwise coordinate, distance from trailing edge of film cooling holes
- $y$  = normal coordinate, distance from the wall
- $z$  = spanwise coordinate, distance from the centerline of the center hole
- $\eta$  = film cooling effectiveness,  $(T_{aw} - T_{\infty}) / (T_{jet} - T_{\infty})$
- $\eta^*$  = approximate unsteady film cooling effectiveness, Eq. (4)
- $\rho$  = density
- $\phi$  = dimensionless temperature,  $(T - T_{\infty}) / (T_{jet} - T_{\infty})$

### Subscripts

- aw = adiabatic wall
- conv = convective
- $f$  = with film cooling
- jet = film cooling jet
- $o$  = without film cooling
- w = wall
- $\infty$  = mainstream

### References

- [1] Varadarajan, K., and Bodard, D. G., 2004, "Effects of Hot Streaks on Adiabatic Effectiveness for a Film Cooled Turbine Vane," ASME Paper No. GT2004-54016.
- [2] Bons, J. P., MacArthur, C. D., and Rivir, R. B., 1994, "The Effect of High Freestream Turbulence on Film Cooling Effectiveness," ASME J. Turbomach., **118**, pp. 814-825.
- [3] Kohli, A., and Bogard, D. G., 1998, "Effects of Very High Free-Stream Turbulence on the Jet—Mainstream Interaction in a Film Cooling Flow," ASME J. Turbomach., **120**, pp. 785-790.
- [4] Ekkad, S. V., Mehendale, A. B., Han, J. C., and Lee, C. P., 1997, "Combined Effect of Grid Turbulence and Unsteady Wake on Film Effectiveness and Heat Transfer Coefficients of a Gas Turbine Blade With Air and CO2 Film Injection," ASME J. Turbomach., **119**, pp. 594-600.
- [5] Burd, S. W., Kaszeta, R. W., and Simon, T. W., 1998, "Measurements in Film Cooling Flows: Hole L/D and Turbulence Intensity Effects," ASME J. Turbomach., **120**, pp. 791-798.
- [6] Funazaki, K., Yokota, M., and Yamawaki, S., 1997, "Effect of Periodic Wake Passing on Film Cooling Effectiveness of Discrete Cooling Holes Around the Leading Edge of a Blunt Body," ASME J. Turbomach., **119**, pp. 292-301.
- [7] Funazaki, K., Koyabu, E., and Yamawaki, S., 1998, "Effect of Periodic Wake Passing on Film Cooling Effectiveness of Inclined Discrete Cooling Holes Around the Leading Edge of a Blunt Body," ASME J. Turbomach., **120**, pp. 70-78.
- [8] Ou, S., Han, J. C., Mehendale, A. B., and Lee, C. P., 1994, "Unsteady Wake Over a Linear Turbine Blade Cascade With Air and CO2 Film Injection: Part

- I—Effect on Heat Transfer Coefficients,” ASME J. Turbomach., **116**, pp. 721–729.
- [9] Mehendale, A. B., Han, J. C., Ou, S., and Lee, C. P., 1994, “Unsteady Wake Over a Linear Turbine Blade Cascade With Air and CO<sub>2</sub> Film Injection: Part II—Effect on Film Effectiveness and Heat Transfer Distributions,” ASME J. Turbomach., **116**, pp. 730–737.
- [10] Jiang, H. W., and Han, J. C., 1996, “Effect of Film Hole Row Location on Film Effectiveness on a Gas Turbine Blade,” ASME J. Turbomach., **118**, pp. 327–333.
- [11] Du, H., Han, J. C., and Ekkad, S. V., 1998, “Effect of Unsteady Wake on Detailed Heat Transfer Coefficients and Film Effectiveness Distributions for a Gas Turbine Blade,” ASME J. Turbomach., **120**, pp. 808–817.
- [12] Du, H., Ekkad, S. V., and Han, J. C., 1999, “Effect of Unsteady Wake With Trailing Edge Coolant Ejection on Film Cooling Performance for a Gas Turbine Blade,” ASME J. Turbomach., **121**, pp. 448–455.
- [13] Teng, S., Sohn, D. K., and Han, J. C., 2000, “Unsteady Wake Effect on Film Temperature and Effectiveness Distributions for a Gas Turbine Blade,” ASME J. Turbomach., **122**, pp. 340–347.
- [14] Teng, S., Han, J. C., and Poinsatte, P. E., 2001, “Effect of Film-Hole Shape on Turbine-Blade Heat-Transfer Coefficient Distribution,” J. Thermophys. Heat Transfer, **15**, pp. 249–256.
- [15] Teng, S., Han, J. C., and Poinsatte, P. E., 2001, “Effect of Film-Hole Shape on Turbine-Blade Film-Cooling Performance,” J. Thermophys. Heat Transfer, **15**, pp. 257–265.
- [16] Heidmann, J. D., Lucci, B. L., and Reshotko, E., 2001, “An Experimental Study of the Effect of Wake Passing on Turbine Blade Film Cooling,” ASME J. Turbomach., **123**, pp. 214–221.
- [17] Wolff, S., Fottner, L., and Ardey, S., 2002, “An Experimental Investigation on the Influence of Periodic Unsteady Inflow Conditions on Leading Edge Film Cooling,” ASME Paper No. GT-2002–30202.
- [18] Adami, P., Belardini, E., Montomoli, F., and Martelli, F., 2004, “Interaction Between Wake and Film Cooling Jets: Numerical Analysis,” ASME Paper No. GT2004–53178.
- [19] Burd, S., and Simon, T. W., 2000, “Effects of Hole Length, Supply Plenum Geometry, and Freestream Turbulence on Film Cooling Performance,” NASA, Report No. CR-2000–210336.
- [20] Schmidt, D. L., Sen, B., and Bogard, D. G., 1996, “Effects of Surface Roughness on Film Cooling,” ASME Paper No. 96-GT-299.
- [21] Pedersen, D. R., Eckert, E. R. G., and Goldstien, R. J., 1977, “Film Cooling With Large Density Differences Between the Mainstream and the Secondary Fluid Measured by the Heat-Mass Transfer Analogy,” ASME J. Heat Transfer, **99**, pp. 620–627.
- [22] Kohli, A., and Bogard, D. G., 1998, “Fluctuating Thermal Field in the Near-Hole Region for Film Cooling Flows,” ASME J. Turbomach., **120**, pp. 86–91.
- [23] Sinha, A. K., Bogard, D. G., and Crawford, M. E., 1991, “Film Cooling Effectiveness Downstream of a Single Row of Holes With Variable Ratio,” ASME J. Turbomach., **113**, pp. 442–449.
- [24] Pietrzyk, J. R., Bogard, D. G., and Crawford, M. E., 1990, “Effect of Density Ratio on the Hydrodynamics of Film Cooling,” ASME J. Turbomach., **112**, pp. 437–443.
- [25] Coulthard, S. M., Volino, R. J., and Flack, K. A., 2006, “Effect of Unheated Starting Lengths on Film Cooling Experiments,” ASME J. Turbomach., **128**, pp. 579–588.
- [26] Coulthard, S. M., Volino, R. J., and Flack, K. A., 2007, “Effect of Jet Pulsing on Film Cooling, Part 1: Effectiveness and Flowfield Temperature Results,” ASME J. Turbomach., **129**, pp. 232–246.
- [27] Coulthard, S. M., Volino, R. J., and Flack, K. A., 2007, “Effect of Jet Pulsing on Film Cooling, Part 2: Heat Transfer Results,” ASME J. Turbomach., **129**, pp. 247–257.
- [28] Sen, B., Schmidt, D. L., and Bogard, D. G., 1996, “Film Cooling With Compound Angle Holes: Heat Transfer,” ASME J. Turbomach., **118**, pp. 800–806.